AIAA JOURNAL
Vol. 38, No. 8, August 2000

Microfluid Dynamics and Acoustics of Resonant Liners

Christopher K. W. Tam* and Konstantin A. Kurbatskii†
Florida State University, Tallahassee, Florida 32306-4510

It is known that most of the acoustic dissipation associated with a resonant liner takes place around the openings of the resonators. However, because the openings are physically very small, there has not been any direct experimental observation of the flow and acoustic fields in this region. As a result, current understanding of liner dissipation mechanisms are either completely theoretical or are based on experiments using much larger physical models. Inasmuch as large openings were used in these experiments, the true Reynolds numbers were unfortunately not reproduced. The flow around and inside a typical liner resonator under the excitation of an incident acoustic field is investigated by direct numerical simulation (DNS). There are two distinct advantages in using DNS. First, by the use of a carefully designed grid, even very small-scale features of the flowfield can be resolved and observed. Second, the correct Reynolds number can be imposed in the simulations. Numerical experiments reveal that at low sound intensity, acoustic dissipation comes mainly from viscous losses in the jetlike unsteady laminar boundary layers adjacent to the walls of the resonator opening. At high sound intensity, dissipation is due to the shedding of microvortices at the mouth of the resonator. The energy dissipation rate associated with the shedding of microvortices is found to be very high. Results of a parametric study of this phenomenon are reported.

I. Introduction

NOWADAYS, acoustic liners are essential for jet engine noise suppression. In the case of resonant liners, the openings of the resonators are usually very small. Because of the small dimensions, the flowfield around the mouth of the resonators has not been directly observed or measured experimentally. This is so despite most acoustic energy dissipation taking place in this region. Present day understanding of the flowfield and dissipation mechanisms of resonant liners are largely theoretical or are based on experiments using much larger scale models. The Reynolds numbers of these large models are, however, not the same as those of the actual resonators of the liner.

At the present time, it is a standard practice to use semi-empirical methods to calculate the impedance of a liner (e.g., Kraft et al.,[1] Hersh and Walker,[2] and Jones[3]). The origin and basic concepts of most of these methods can be traced back to the work of Melling.[4] Melling recognized that, depending on the sound-pressure level (SPL), a liner can behave linearly or nonlinearly. In the linear regime, the flow at the opening of a resonator is assumed to be laminar and parallel. These assumptions are true for flows in long tubes at low Reynolds number. On starting from these assumptions, Melling presented analysis to show that the dissipative or resistive losses may be of the Poiseuille type or the Helmholtz type (the latter being frequency dependent). Essentially, the losses come about because of viscous dissipation in the shear layer, as shown in Fig. 1a. Because the flow passage in the opening of the resonator has a finite length, an end correction[5,6] was added to account for the extra losses. In the nonlinear regime, it is generally assumed that a turbulent jet forms at the mouth of the resonator, as shown in Fig. 1b. Early experimental observations by Ingard and Labate[7] and Ingard and Ising[8] on flow from relatively large orifices appeared to provide the basis for the turbulent jet model. The turbulent jet model was adopted in the theoretical work of Sirignano[9] and Zinn.[10] The observation of jetting was reported by Hersh and Walker[2] (but we are unable to find the size of the orifice in their experiment). When a turbulent jet is formed, the primary mechanism of dissipation is turbulence. In the semi-empirical approach, most investigators employed a discharge coefficient to lump all of the turbulence dissipation into a single unknown. There is, however, no generally accepted method to find the value of the discharge coefficient.

The primary objective of this investigation is to obtain a better understanding of the flowfield and physics around the opening of a liner resonator when excited by incident acoustic waves. Specifically, we are interested in the mechanisms by which the acoustic energy is dissipated. We will investigate both the linear and the nonlinear regime. It is also our plan to perform a parametric study of the effects of frequency, intensity, and angle of incidence of the incident sound waves on the flowfield.

To accomplish our objectives, we will perform direct numerical simulation of the flowfield around and inside a liner resonator under the excitation of plane acoustic waves. Unlike physical experiments, the smallness of the opening of the resonator is not a hindrance to our numerical simulation. There are two distinct advantages in using direct numerical simulation. The first advantage is that by using a well-designed computation mesh, it is possible to resolve and to observe even very small-scale features of the flow. This will allow us to make a precise estimate of the viscous dissipation rate. Second, we can impose the correct Reynolds number in the numerical experiments. This avoids the basic mismatch of Reynolds number problem when using a much larger model in a physical experiment. To ensure that the numerical simulation is of high quality, the seven-point stencil dispersion-relation-preserving (DRP) scheme[11] is used. The DRP scheme is a computational aeroacoustics method designed to minimize numerical dispersion and dissipation.[12] The scheme has been applied successfully even to the screech tone problem[13] in which very small-amplitude sound waves were captured in the presence of supersonic flows and shock waves. Good agreement was found between the computed screech tone frequencies and intensities with experimental measurements.

The mathematical model and the mesh distribution will be presented in Sec. II of this paper. The observed flowfield around the resonator and the measured dissipation rate under the excitation of low-intensity acoustic waves are reported in Sec. III. The flow in the channel of the resonator opening is not in the form of a slug flow as suggested by Melling[4] and others. The unsteady boundary-layer flow has jetlike velocity profiles, which are responsible for most of the viscous dissipation. In Sec. IV, the case of high-SPL is reported. The observation of a new dissipation mechanism due to the shedding of microvortices is presented. The mechanism is extremely efficient. In all our simulations, even at sound level as high as 160 dB, a turbulent jet flow at the mouth of the resonator has never been observed. This differs from the experimental

Received 8 May 1999; presented as Paper 99-1850 at the AIAA/CEAS 5th Aeroacoustics Conference, Bellevue, WA, 10–12 May 1999; revision received 15 September 1999; accepted for publication 1 October 1999.

*Distinguished Research Professor, Department of Mathematics. Associate Fellow AIAA.

†Postdoctoral Research Associate, Department of Mathematics.

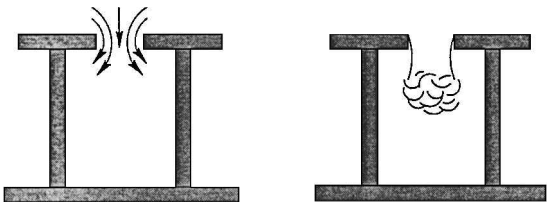

a) Wall friction b) Turbulent jet

Fig. 1 Dissipation mechanisms: a) low sound intensity and b) high sound intensity.

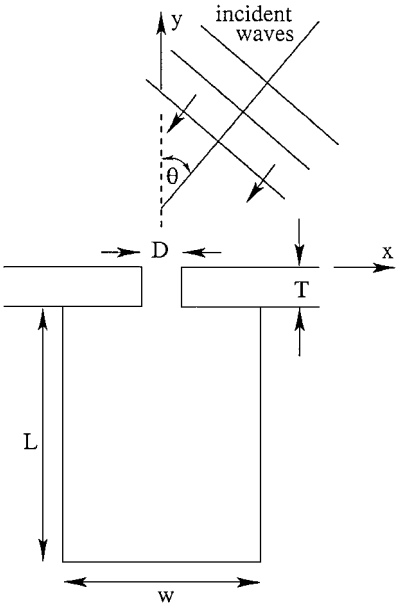

Fig. 2 Mathematical model used in numerical simulation.

observations of Ingard and Labate[7] and Ingard and Ising.[8] We believe that the difference is a matter of Reynolds number. A more detailed discussion is provided in the conclusion section of this paper.

II. Mathematical Model, Grid Design, and Computational Algorithm

A. Mathematical Model

We will consider the case of a single resonator in a static environment. By the use of this model, it is implicitly assumed that the resonators of the liner are sufficiently far apart that there is no mutual interaction. Essentially, we are interested to find the microfluid flowfield of a two-dimensional resonator induced by incident plane acoustic waves as shown in Fig. 2.

Typical dimension of the resonator opening, D, is quite small. For this reason, the viscous effect is anticipated to be important near the mouth of the resonator. The governing equations are the compressible Navier–Stokes and energy equations. In dimensionless form with length scale equal to D (the width of the resonator opening), velocity scale equal to a_∞ (the sound speed), time scale equal to D/a_∞, density scale equal to ρ_∞ (ambient gas density), and pressure and stress scale equal to $\rho_\infty a_\infty^2$, these equations may be written as

$$\frac{\partial \rho}{\partial t} + \rho \frac{\partial u_j}{\partial x_j} + u_j \frac{\partial \rho}{\partial x_j} = 0 \tag{1}$$

$$\frac{\partial u_i}{\partial t} + u_j \frac{\partial u_i}{\partial x_j} = -\frac{1}{\rho}\frac{\partial p}{\partial x_i} + \frac{1}{\rho}\frac{\partial \tau_{ij}}{\partial x_j} \tag{2}$$

$$\frac{\partial p}{\partial t} + u_j \frac{\partial p}{\partial x_j} + \gamma p \frac{\partial u_j}{\partial x_j} = 0 \tag{3}$$

$$\tau_{ij} = \frac{1}{Re_D}\left(\frac{\partial u_i}{\partial x_j} + \frac{\partial u_j}{\partial x_i}\right) \tag{4}$$

where

$$Re_D = Da_\infty / \nu$$

is the Reynolds number. On the walls, the no-slip boundary conditions are to be enforced.

The amplitude of the incident plane acoustic waves (Fig. 2) is assumed to be small. It is given by the solution of the linearized Euler equations. We will use a superscript i for the incident sound waves and r for the reflected waves in the absence of the resonator. These waves are given by

$$\begin{bmatrix} \rho^i \\ u^i \\ v^i \\ p^i \end{bmatrix} = \begin{bmatrix} 1 \\ -\sin\theta \\ -\cos\theta \\ 1 \end{bmatrix} A\cos[-\omega(x\sin\theta + y\cos\theta + t)] \tag{5}$$

$$\begin{bmatrix} \rho^r \\ u^r \\ v^r \\ p^r \end{bmatrix} = \begin{bmatrix} 1 \\ -\sin\theta \\ \cos\theta \\ 1 \end{bmatrix} A\cos[\omega(-x\sin\theta + y\cos\theta - t)] \tag{6}$$

where (u, v) are the velocity components in the (x, y) directions, θ is the angle of incidence, and ω is the angular frequency. A is the amplitude of the incident sound waves. At 15°C, A is related to the decibel level by

$$A = 10^{\mathrm{dB}/20 - 9.701} \tag{7}$$

B. Grid Design

The present problem is one with large disparate length scales. Away from the opening of the resonator, viscosity is unimportant. In these inviscid regions, both outside and inside the resonator, the length scale is the acoustic wavelength λ. Adjacent to the walls at the opening of the resonator, thin unsteady viscous wall layers would develop. The thickness of these layers, δ, is much smaller than the width of the opening, that is, $D \gg \delta$. For jet engine liners, the acoustic wavelength λ is much larger than D. Thus, there is a length scale difference of an order of magnitude or more given by

$$\lambda \gg D \gg \delta \tag{8}$$

To provide adequate local spatial resolution needed in different regions of the physical domain, a special grid design becomes necessary.

Figure 3 shows the computation domain used in the simulations. The size of the domain outside the resonator is determined by the requirement that the resonator is at least about one wavelength away from the boundary at the lowest frequency of interest and more than two but not more than three wavelengths away at the resonance frequency. The one wavelength requirement is to ensure that the boundary of the computation domain is in the nominally far field of any acoustic disturbances generated by the resonator. The three wavelengths requirement is to avoid an excessively large domain leading to long computer run time.

Figure 4 gives the mesh size distribution inside and at the opening of the resonator. A square mesh is used everywhere. There are six

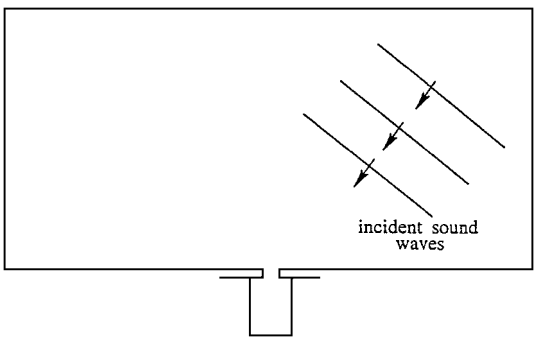

Fig. 3 Computational domain.

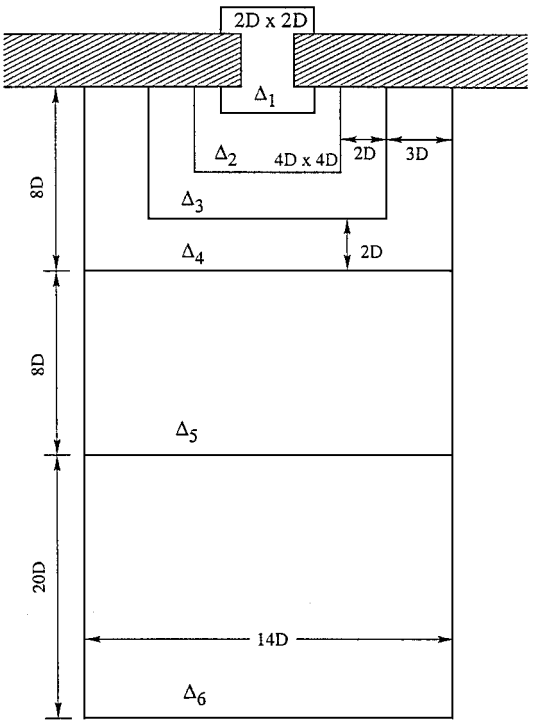

Fig. 4 Grid distribution inside and at the mouth of the resonator; mesh size: $\Delta_1 = 0.0125D$, $\Delta_n = 2^{n-1}\Delta_1$, $n = 2, \ldots, 6$.

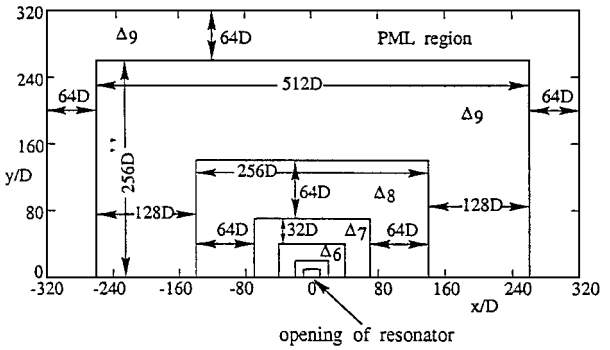

Fig. 5 Grid distribution outside the resonator; mesh size: $\Delta_1 = 0.0125D$, $\Delta_n = 2^{n-1}\Delta_1$, $n = 2, \ldots, 9$.

blocks shown in Fig. 4. The block located right at the opening of the resonator has the finest mesh with size $\Delta_1 = 0.0125D$. The mesh size of each adjacent block increases by a factor of 2 in the direction going away from the opening. Thus, the block with mesh size Δ_n has an actual size equal to $2^{n-1}\Delta_1$. We will use the seven-point DRP scheme in the computation. This scheme has a spatial resolution of seven mesh points per wavelength. Therefore, based on the largest mesh size used inside the resonator, we are confident that the mesh design of Fig. 4 can adequately resolve up to the 5th transverse and the 12th longitudinal standing acoustic modes of the resonator.

Figure 5 provides the grid distribution outside the resonator. There are eight blocks surrounding the block with the finest mesh at the mouth of the resonator. Again the mesh size of the adjacent block increases by a factor of 2 as indicated. The largest mesh size is $2^8 = 256$ times that of the smallest mesh or 3.2 times the size of the resonator opening. As noted before, viscous effect is unimportant away from the mouth of the resonator. Accordingly, in our computer code, the viscous terms of Eqs. (1–3) are dropped except in the blocks with the five smallest mesh sizes. In other words, the Euler equations instead of the Navier–Stokes equations are solved in the blocks with coarse meshes.

C. Computational Algorithm

Equations (1–4) are discretized according to the seven-point stencil DRP scheme.[11,12] To eliminate spurious numerical waves, artificial selective damping terms are added as suggested in Refs. 12 and 14. For instance, the x-momentum equation of Eq. (2), after discretization in two steps, has the form

$$K^{(n)}_{\ell,m} = -\frac{u^{(n)}_{\ell,m}}{\Delta x}\sum_{j=-3}^{3} a_j u^{(n)}_{\ell+j,m} - \frac{v^{(n)}_{\ell,m}}{\Delta y}\sum_{j=-3}^{3} a_j u^{(n)}_{\ell,m+j} + \frac{1}{\rho^{(n)}_{\ell,m}}\left\{\frac{1}{\Delta x}\sum_{j=-3}^{3} a_j\left(-p^{(n)}_{\ell+j,m} + (\tau_{xx})^{(n)}_{\ell+j,m} + \frac{\Delta x}{\Delta y}(\tau_{xy})^{(n)}_{\ell,m+j}\right)\right\} - \frac{1}{Re_\Delta \Delta x}\sum_{j=-3}^{3} d_j\left(u^{(n)}_{\ell+j,m} + u^{(n)}_{\ell,m+j}\right) \tag{9}$$

$$u^{(n+1)}_{\ell,m} = u^{(n)}_{\ell,m} + \Delta t\sum_{j=0}^{3} b_j K^{(n-j)}_{\ell,m} \tag{10}$$

where ℓ and m are the spatial indices in the x and y directions and superscript n is the time level. $Re_\Delta = \Delta a_\infty / \nu_a$ is the artificial mesh Reynolds number, and Δ is the local mesh size in physical units. The last term of Eq. (9) is the artificial selective damping term.[12,14] By the taking of the Fourier transform of the viscous and artificial damping terms of Eq. (9), it is easy to find that the ratio of the magnitude of the molecular viscosity term to the artificial damping term is given by

$$\frac{\text{viscosity term}}{\text{artificial damping term}} \simeq \frac{D}{\Delta}\frac{Re_\Delta}{Re_D}\frac{(\bar{\alpha}\Delta x)^2}{\tilde{D}(\alpha\Delta x)} \tag{11}$$

where α is the wave number, $\bar{\alpha}$ is the stencil wave number,[11,12] $Re_D = a_\infty D/\nu$ is the Reynolds number of the opening, and $\tilde{D}(\alpha\Delta x)$ is the artificial selective damping function[12,14] given by

$$\tilde{D}(\alpha\Delta x) = \sum_{j=-3}^{3} d_j e^{-ij\alpha\Delta x} \tag{12}$$

Figure 6 is a plot of Eq. (11) as a function of $\alpha\Delta x$ for the block with the finest mesh at the opening of the resonator. As can be seen, over the resolved wave number range, the artificial selective damping is small compared to the molecular viscous damping. However, for large wave numbers, the artificial selective damping is much larger. It is, therefore, capable of removing efficiently short spurious numerical waves without affecting the effect of viscosity on the physical solution.

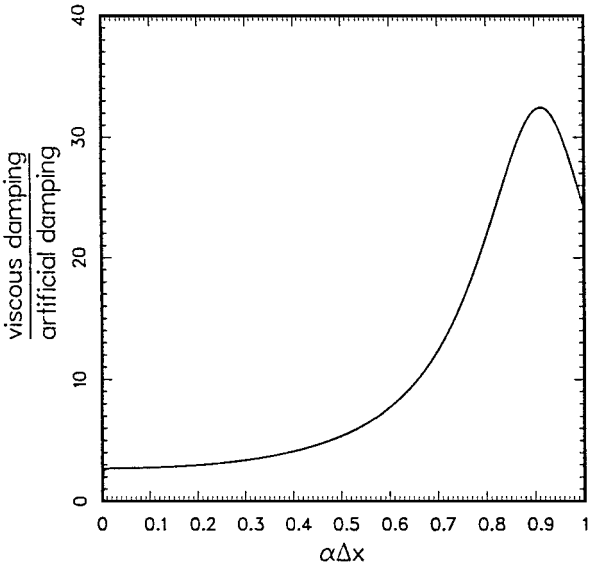

Fig. 6 Ratio of viscous damping to artificial damping as a function of wave number for the finest mesh block, $\Delta x = D/80$, $Re_\Delta = 20$, and $Re_D = 470$.

The change in mesh size between two computation blocks requires the use of special stencils for mesh points in the buffer region. To avoid unnecessary computation, the local time step Δt also changes by a factor of 2 between adjacent blocks in exactly the same way as the mesh size. A more detailed description of this multi-size-mesh, multi-time-step algorithm is provided in the Appendix. This algorithm, which uses nearly the most optimal local time step, is extremely efficient. Because of a numerical stability requirement, the time step of most standard algorithms using a single Δt is restricted by that of the finest mesh. This leads to wasteful computations over the regions with larger mesh sizes.

On the wall surfaces, inside and outside the resonator, the ghost point method[15] is used to enforce the wall boundary conditions. We use the no-slip boundary conditions along the walls adjacent to the computation blocks with the two smallest meshes. For the remaining walls, the zero normal velocity boundary condition is enforced.

Along the artificial outside boundaries of the computation domain (see Figs. 3 and 5), a special set of boundary conditions is required. These boundary conditions perform two very different functions. First, it must generate the incident and the reflected waves (the wave system above the flat wall outside the resonator) as if the domain is semi-infinite. This wave system is given by the direct sum of Eqs. (5) and (6) together with the mean density and pressure. Let us use a superscript t to denote this total wave field. It is straightforward to find

$$\begin{bmatrix} \rho^t \\ u^t \\ v^t \\ p^t \end{bmatrix} = \begin{bmatrix} 1 \\ 0 \\ 0 \\ 1/\gamma \end{bmatrix} + 2A \begin{bmatrix} \cos(\omega y \cos\theta)\cos[\omega(x\sin\theta + t)] \\ -\sin\theta\cos(\omega y\cos\theta)\cos[\omega(x\sin\theta + t)] \\ \cos\theta\sin(\omega y\cos\theta)\sin[\omega(x\sin\theta + t)] \\ \cos(\omega y\cos\theta)\cos[\omega(x\sin\theta + t)] \end{bmatrix} \tag{13}$$

Second, the boundary conditions must allow the acoustic disturbances generated by the resonator to leave the computation domain without reflection. In this work, we use the split variable method.[16] A perfectly matched layer (PML)[17] is used at the outermost mesh block of the computation domain. All of the dependent variables in this region are split into two parts. One part is given by the wave system of Eq. (13). The other part is computed according to the equations of the PML. The PMLs absorb all of the outgoing acoustic waves without reflection. Because a seven-point stencil is used in the computation, the stencils of some of the interior points extend over to the PML region. These stencil points pick up the wave system given by Eq. (13). In this way, the desired wave system is generated automatically.

It is known that spurious numerical waves are usually generated at the boundaries of the computation domain. If ignored, these waves could lead to numerical instability. To suppress the generation of these spurious waves, additional artificial selective damping terms, beyond those needed for general background damping discussed before, are added around the boundaries of the computation domain shown in Fig. 3. In this work, we follow the scheme used in Ref. 13. Special treatment of corner points employed in Ref. 13 is also adopted here for the four corner points at the opening of the resonator.

III. Flowfield Excited by Low-Intensity Sound

In this section, the results of our direct numerical simulation of the flow and acoustic fields of the resonator under the excitation of low-intensity sound waves are reported. Throughout this work, the dimensions of the resonator (see Fig. 2) are taken to be

$$D = T = 0.8\,\text{mm}, \qquad L = 36D, \qquad W = 14D \tag{14}$$

The temperature is 15°C. The speed of sound and the kinematic viscosity of air are 340 m/s and 0.145 cm^2/s, respectively. Based on the depth of the resonator, the quarter-wave resonance frequency is approximately 3 kHz.

In all of the simulations, Eq. (13) is used as the initial condition outside the resonator. Inside the resonator, the initial condition used is

$$p = 1/\gamma, \qquad \rho = 1, \qquad u = v = 0 \tag{15}$$

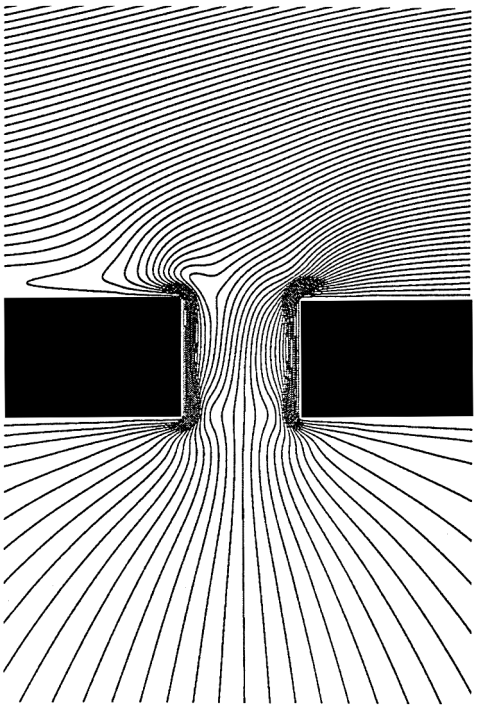

Fig. 7a Instantaneous streamline pattern at the mouth of the resonator; SPL = 120 dB, f = 3 kHz, and θ = 30 deg.

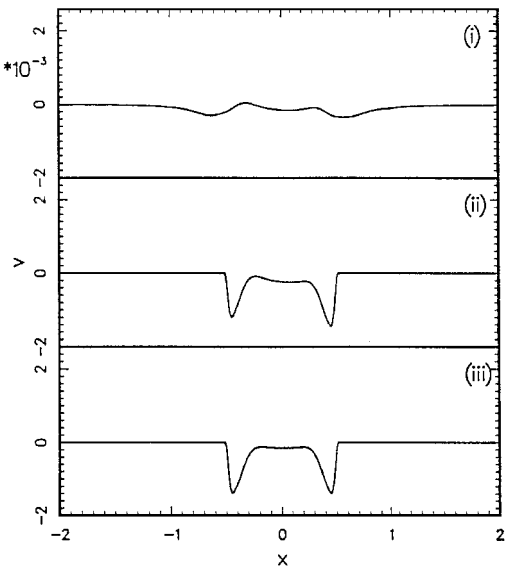

Fig. 7b Instantaneous velocity distribution (v component) near the mouth of the resonator: i) along y = 0.2, ii) along y = 0.0, and iii) along y = − 1.0.

The numerical solution is marched in time until the transient disturbances have left the computation domain. All of the observations and measurements reported here are made after a time periodic state is established in the computation domain.

Figure 7a shows the instantaneous streamline pattern around the opening of the resonator at 120-dB incident SPL and 3-kHz frequency. The angle of incidence is 30 deg. The flow is laminar and unsteady. Figure 7b shows the v-velocity profile at three levels. The top figure is at $y = 0.2$, which is slightly above the opening. The middle and bottom figures are at the top and bottom of the opening. Of interest is the jetlike velocity profile adjacent to the walls of the opening. This velocity profile is quite different from that given by Melling.[4] It is certainly not slug flow as assumed by some past investigators. The u-velocity profiles at the two sides of the opening are provided in Fig. 8. There are strong jetlike boundary layer flows along the face sheets into the opening on top and out of the opening

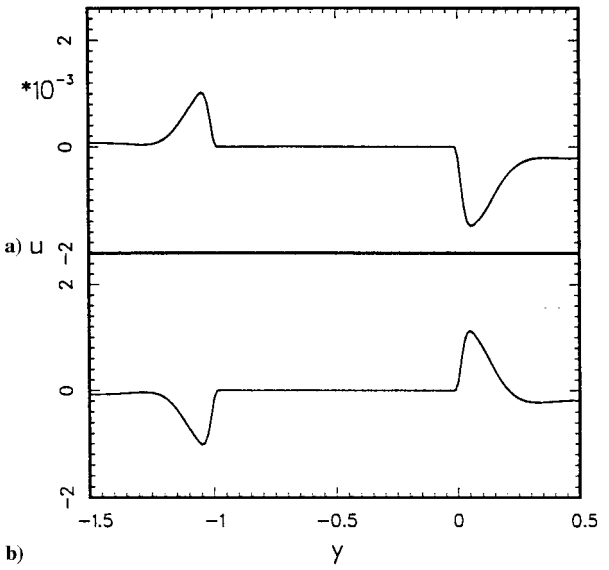

Fig. 8 Instantaneous u-velocity profile at the beginning of a cycle; SPL = 120 dB, f = 3 kHz, and θ = 30 deg: a) along the line x = 0.5 and b) along the line $x = -0.5$.

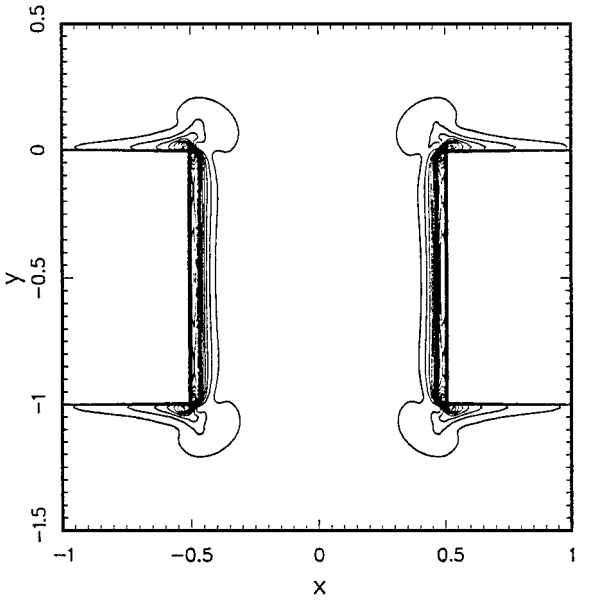

Fig. 9 Contours of time-averaged dissipation rate.

on the bottom. During a part of the cycle, the flow in the center of the opening reaches the same velocity as in the boundary layer giving a fairly uniform velocity profile. Then the jetlike boundary-layer flow reappears as the flow reverses itself during the next half-cycle.

The purpose of an acoustic liner is to dissipate the energy of the incident acoustic waves. With the velocity field determined, it is straightforward to calculate the rate of energy dissipation due to viscosity. The time-averaged dissipation rate at (x, y), $\bar{D}(x, y)$, is given by (in dimensional units)

$$\bar{D}(x, y) = \frac{1}{T}\int_0^T \sigma_{ij}\frac{\partial u_i}{\partial x_j}\,\mathrm{d}t \tag{16}$$

where

$$\sigma_{ij} = \mu\left(\frac{\partial u_i}{\partial x_j} + \frac{\partial u_j}{\partial x_i}\right)$$

and T is the period of oscillation. Figure 9 shows a contour map of $\bar{D}(x, y)$ in the region at the mouth of the resonator. As expected, most of the energy dissipation takes place adjacent to the walls of the opening of the resonator. The shear gradient of the jetlike boundary-layer flows is responsible for most of the dissipation. The total energy dissipation rate E_{viscous} may be found by integrating Eq. (16) over the mouth region of the resonator:

$$E_{\text{viscous}} = \iint_{\text{resonator}} \bar{D}(x, y)\,\mathrm{d}x\,\mathrm{d}y \tag{17}$$

The energy flux of the incident acoustic waves through an area equal to the opening of the oscillator is equal to

$$E_{\text{incident}} = \overline{p^2 D}\,|\ \rho_\infty a_\infty \tag{18}$$

where an overbar indicates the time average. The measured value from the numerical simulation yields $E_{\text{viscous}}/E_{\text{incident}} = 0.57$. In other words, about 60% of the acoustic energy flux is dissipated. This is a typical value at low incident sound intensity. Thus, in the linear regime, the dissipation rate is low.

IV. Flowfield Excited by High-Intensity Sound

When the incident SPL is increased to 150 dB, the flow around the opening of the resonator changes drastically. The flow pattern is quite unexpected. The phenomenon is neither laminar nor turbulent. It is slightly chaotic and aperiodic, a state somewhere between laminar and turbulent.

A. Phenomenon of Vortex Shedding

Under high-intensity incident sound waves, the shedding of microvortices occurs at the opening of the resonator. Figure 10 shows the instantaneous streamline pattern of the flowfield at 150-dB SPL and 3-kHz frequency. The closed streamlines represent vortices. These vortices are shed from the corners of the opening. A careful examination of the time simulations reveals that there are two ways by which these microvortices are shed. Internal shedding (Fig. 11a) takes place when the flow separates from a corner on the side of the

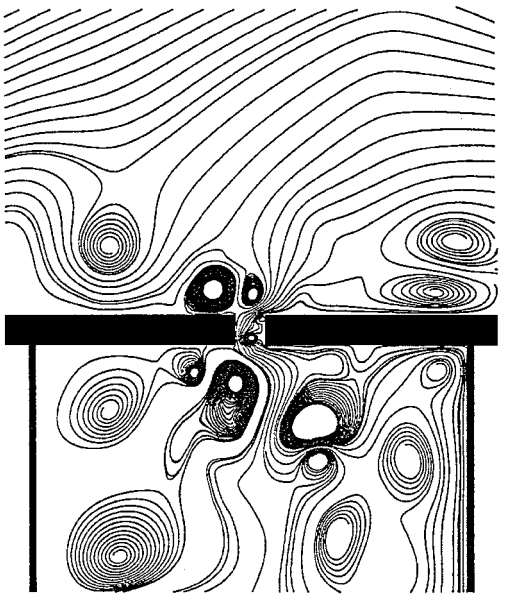

Fig. 10 Instantaneous streamline pattern showing the shedding of microvortices at the mouth of the resonator; SPL = 150 dB, frequency = 3 kHz, θ = 30 deg; size of the opening = 0.8 × 0.8 mm and size of resonator = 1.12 × 2.88 cm.

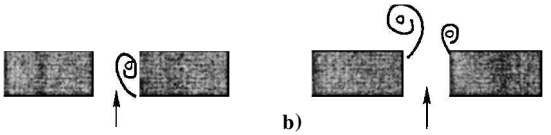

Fig. 11 Vortex shedding at the corners of the mouth of the resonator: a) internal shedding leading to attached vortices and vortex merging and b) external shedding leading to free vortices.

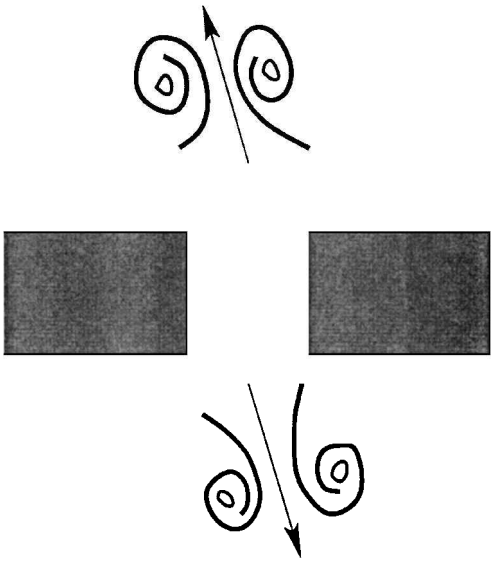

Fig. 12 Counter-rotating vortex pairs moving away from the mouth of the resonator.

opening with incoming flow. The shed vortices are trapped inside the mouth of the resonator. Generally the vortices are attached to the wall. They sometimes merge with other vortices. Sometimes, they simply dissipate and vanish by themselves. Internally shed vortices rarely break free from the walls to form detached or free vortices. External shedding (Fig. 11b) takes place when flow separates from a corner on the side of the opening with outgoing flow. External shedding usually leads to free vortices. Many of these vortices can be seen in Fig. 10.

In the absence of a mean flow, a free vortex cannot move away from the resonator opening. To move away, two vortices would form a counter-rotating pair as shown in Fig. 12. Each vortex of the pair is moved by the rotational velocity associated with the circulation of its partner. A thorough review of the flowfield of the numerical simulations indicates that this is the main mechanism by which shed vortices move out of the resonator opening region.

With vortex shedding, the flow velocity at the resonator opening is extremely high. Figure 13a shows an enlarged instantaneous streamline pattern of the shedding of micro-vortices. Figure 13b shows the v-velocity distribution along the centerline of the opening. In the presence of strong vortices, the v-velocity component may reach an instantaneous value as high as 0.1–0.2 Mach number. This is very high flow velocity.

B. Shedding of Microvortices as a Dissipation Mechanism

Each shed microvortex carries with it a certain amount of kinetic energy. This energy comes originally from the incident acoustic waves. The kinetic energy associated with the rotational motion of the vortex cannot be converted back into acoustic wave energy. It is dissipated into heat through viscosity. In this way, the shedding of microvortices becomes a significant dissipation mechanism.

To determine the efficiency of this dissipation mechanism, we measured the rotational velocity v_θ of a number of free vortices from our numerical simulations. Figure 14 is a typical distribution of the rotational velocity as a function of the radial distance from the center of the microvortex at 150-dB SPL and 3-kHz frequency. The averaged kinematic energy of the vortex per unit span, K, is given by

$$K = \pi \int_0^R \rho(r) v_\theta^2(r) r \, dr \tag{19}$$

where R is the size of the vortex. By counting the number of shed free vortices over a long period of time, the averaged number of vortices shed per oscillation period, N, is easily determined. The shedding frequency is equal to N/T, where T is the period. The rate of energy dissipation is given by

$$E_{\text{shedding}} = KN/T$$

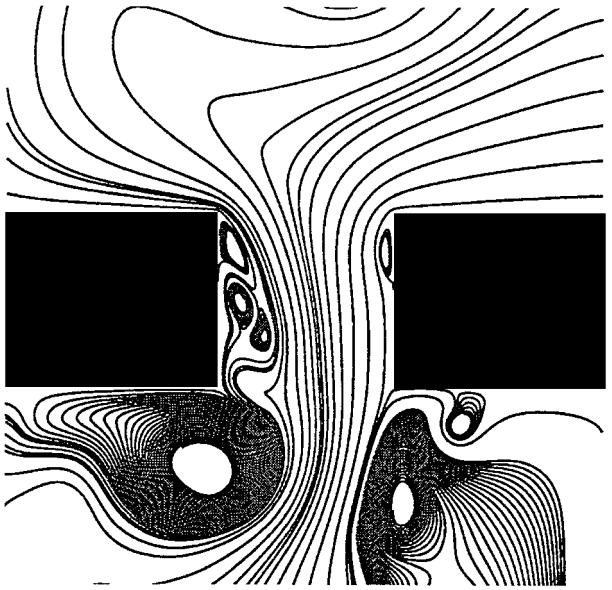

Fig. 13a Instantaneous streamline pattern showing the shedding of microvortices at the mouth of the resonator.

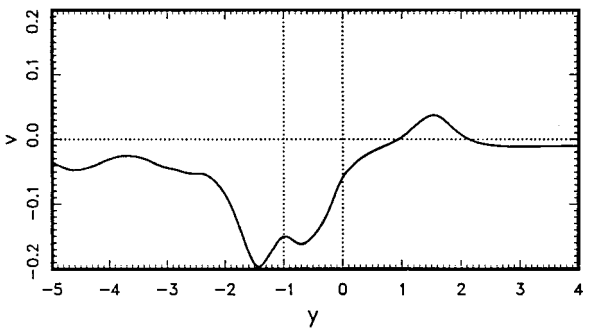

Fig. 13b Instantaneous velocity distribution (v component) along the centerline of the opening of the resonator; incident sound wave SPL = 150 dB, f = 3 kHz, and θ = 30 deg.

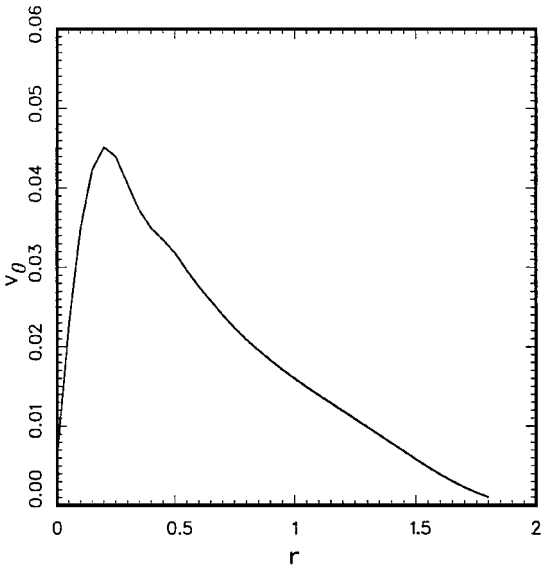

Fig. 14 Typical v_θ distribution of a microvortex.

For the case of incident sound at 150 dB, 3 kHz, and θ (the angle of incidence) = 30 deg, it is found that $N = 6.4$. The ratio of the energy dissipation rate by vortex shedding to the energy flux rate of the incident acoustic wave on an area equal to the opening of the resonator, $E_{\text{shedding}}/E_{\text{incident}}$, is found to be equal to 7.5. (Note that a useful interpretation of the ratio $E_{\text{shedding}}/E_{\text{incident}}$ is to pretend that we are dealing with light instead of sound. E_{incident} is then the rate at which incident wave energy falls into a hole of width D and is

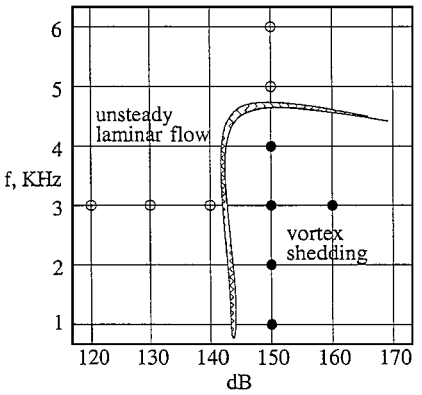

Fig. 15 Boundary between vortex shedding and no vortex shedding in the frequency-sound intensity plane: ●, vortex shedding and ⊘, no vortex shedding; resonance frequency of resonator = 3 kHz.

absorbed. Now with vortex shedding, we find $E_{\text{shedding}} = 7.5 E_{\text{incident}}$. This suggests that effectively the hole appears to be 7.5 times larger than its physical size. Of course, this is possible because the sound waves have a wavelength much larger than the opening and do not behave like light waves.) On comparing this with the dissipation rate due to viscosity, the vortex shedding mechanism is about 12.5 times more efficient. Thus, an acoustic liner is most effective when there is vortex shedding.

C. Parametric Study of the Vortex Shedding Phenomenon

A parametric study of the vortex shedding phenomenon was carried out. The resonator has dimensions given by Eq. (14). Our first objective was to determine the frequency and SPL at which vortex shedding would occur and also their sensitivity to the angle of incidence. Figure 15 gives the boundary between vortex shedding and no vortex shedding in the frequency–SPL (in decibel) plane. As can be seen, vortex shedding occurs when the frequency of the incident sound waves is near but not necessarily at the resonance frequency. However, the SPL must be sufficiently high indicating that the phenomenon is highly nonlinear.

The vortex shedding phenomenon appears to be not sensitive to the angle of incidence. This is, perhaps, not surprising. Because the size of the resonator opening is much smaller than an acoustic wavelength, the resonator sees essentially a time fluctuating field outside, irrespective of its original direction of propagation. Moreover, the effectiveness of vortex shedding as a dissipation mechanism of acoustic energy is also only weakly dependent on the angle of incidence. Let E be the total energy dissipation rate, that is, it is the sum of the rate of energy dissipation by vortex shedding and that by viscosity around the mouth region of the resonator. Suppose E_i to be the energy flux rate of the incoming sound on an area equal to that of the opening of the resonator. The ratio E/E_i is a measure of the effectiveness of the resonator in dissipating acoustic energy. Figure 16 shows the variation of E/E_i with the angle of incidence at incident sound SPL of 150-dB SPL and 3-kHz frequency. There is only a small difference between normal and grazing incidence. There is vortex shedding irrespective of the angle of incidence.

The dependence of E/E_i on the frequency of sound at 150-dB SPL and 30-deg angle of incidence is shown in Fig. 17. Figure 17 indicates clearly that the effectiveness of energy dissipative is sensitive to frequency. Impressive dissipative rate occurs only over a relatively narrow frequency band. The band of frequency depends on the size of the resonator. However, even at frequencies at which the value of E/E_i is not as fantastic, there is still far larger dissipation by the vortex shedding mechanism than by the unsteady oscillating shear layer mechanism of the linear regime.

Figure 18 shows the dependence of E/E_i on sound intensity. The frequency of the incident sound wave is fixed at 3 kHz, the quarter-wave resonance frequency. At and below 140 dB, there is no vortex shedding. As a result, the dissipation rate is extremely low. At and above 150 dB, strong vortex shedding occurs. This causes large energy dissipation. The large difference in E/E_i between 140 and 150 dB is associated with the almost abrupt change

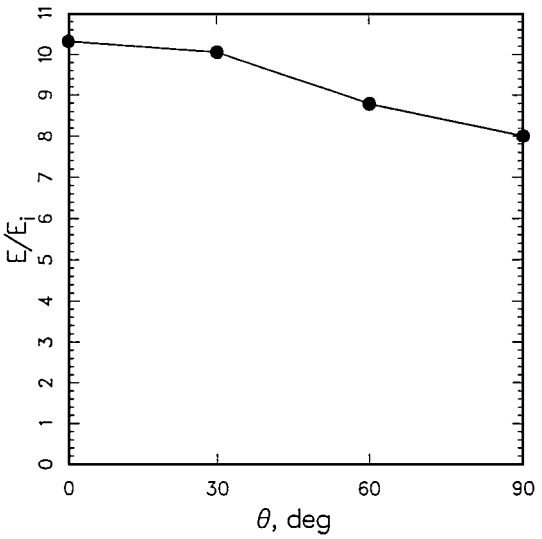

Fig. 16 Variation of energy dissipation rate with angle of incidence at 150-dB SPL and $f = 3$ kHz.

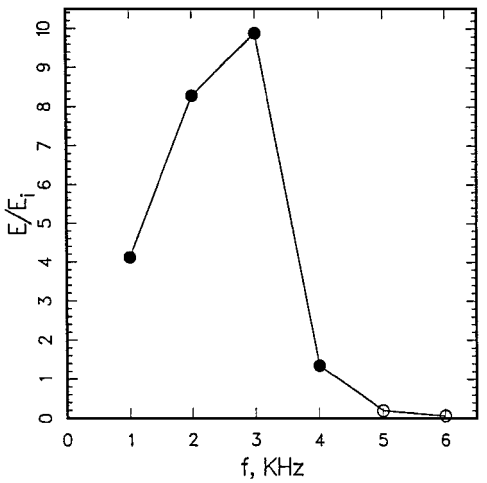

Fig. 17 Variation of energy dissipation rate with frequency of incident sound wave; SPL = 150 dB, $\theta = 30$ deg: ●, with vortex shedding and ⊘, no vortex shedding.

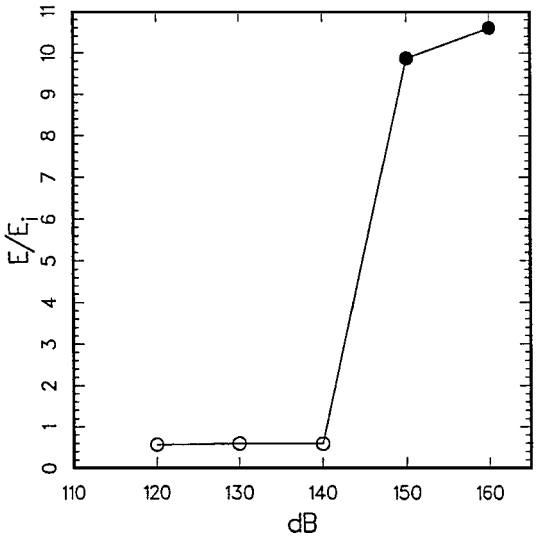

Fig. 18 Variation of energy dissipation rate with incident acoustic wave intensity; $f = 3$ kHz, $\theta = 30$ deg: ●, vortex shedding and ⊘, no vortex shedding.

in the flowfield around the mouth of the resonator. The large dissipation is maintained at 160 dB, which is the highest SPL used in our numerical simulations.

V. Conclusion

The physical size of the holes of a typical jet engine liner is so small that, as far as is known, the flowfield around them has never been observed experimentally. In the past, semi-empirical models of the flowfield had been developed. They were used to predict the impedance properties of the liners. These models were either formulated theoretically or based on experiments in which much larger size models were used. Because of the size difference, the correct Reynolds number was not reproduced in these experiments.

In this work, the microfluid dynamics of a typical liner resonator under acoustic excitation is investigated by direct numerical simulation. It is to be emphasized that the small physical size of the liner holes presents no hindrance to numerical simulation. The correct Reynolds number is imposed in all of the simulations. Results of the present simulations appear to be quite different from what was conjectured theoretically or observed experimentally using larger scale models. At low sound intensity, we observe strong oscillatory boundary layer with jetlike velocity profile around the resonator opening. Most of the dissipation is contributed by the shear gradients of the unsteady boundary-layer flows.

At high sound intensity, we observe the shedding of microvortices from the mouth of the resonator. These microvortices carry with them a significant amount of kinetic energy that is eventually dissipated into heat. Our measurements have shown that the shedding of microvortices is a very efficient energy dissipation mechanism. It is definitely a desirable feature of an acoustic liner. We found that the angle of incidence of incoming sound waves is not a sensitive parameter of the vortex shedding phenomenon. On the other hand, vortex shedding occurs only when the incident SPL exceeds a certain critical value and only at a selected band of frequencies. This band depends on the size of the resonator.

Note that we have performed direct numerical simulations up to an SPL of 160 dB. Yet, we have not seen the formation of an oscillatory turbulent jet at the opening of the resonator as had been proposed by a number of investigators[2,7–10] in the past. That formation of an oscillatory turbulent jet does not take place even at 160-dB SPL suggests that it is probably not a good model for liners with hole size typical of those in current use.

The present work is one of the first applications of computational aeroacoustics methods to the study of acoustic liners. Because of this, our scope is quite limited. We have considered only a two-dimensional model without outside flow. However, even with these limitations, our simulations have been able to provide new and useful insight into the flow physics and dissipation mechanisms of acoustic liners. We believe computational aeroacoustics is an extremely useful and powerful tool for liner impedance prediction and design. In our future work, we plan to add an external flow outside the liner and to extend the resonator model to three dimensions.

Appendix: Multi-Size-Mesh, Multi-Time-Step Computation Algorithm

An efficient way to compute the solutions to problems with large disparate length scales is to use different size mesh in different region of the computation domain.[18] Because the time-marching step Δt is, by numerical stability requirement, proportional to the mesh size, an optimum computation scheme should, therefore, use different time steps in different regions as well. In the present scheme, the mesh size of the adjacent region increases by a factor of 2 as shown in Fig. A1. There is a corresponding increase in the time step. Because of the change in mesh size, special spatial stencils have to be used for the three columns or rows of mesh points adjacent to the mesh change line on the fine mesh side (Fig. A1). To lock the step in time, intermediate values of the unknowns at the half time step in the coarse mesh region are also needed (Fig. A2). Therefore, a special time-marching stencil that advances the solution by a half time step becomes necessary. The coefficients of these stencils can be found by the optimization procedure introduced by Tam and Webb.[11] They are listed next together with the coefficients of the appropriate damping stencils.

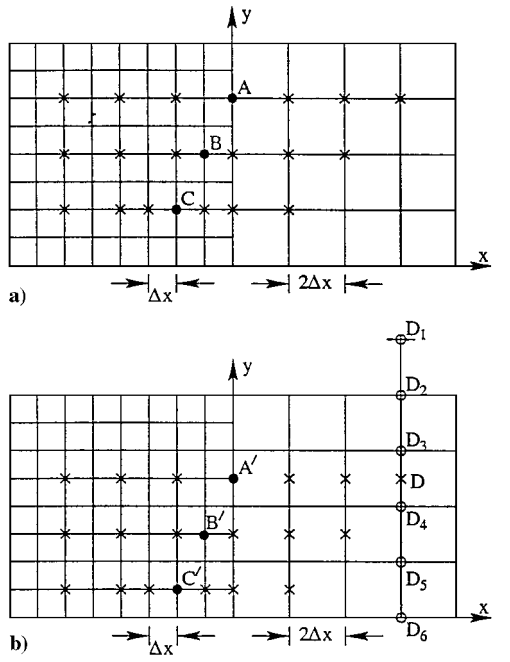

Fig. A1 Spatial stencils for points adjacent to the mesh size change line: ●, points at which spatial derivatives are to be approximated by finite difference; ×, stencil points; and ⊘, interpolation points.

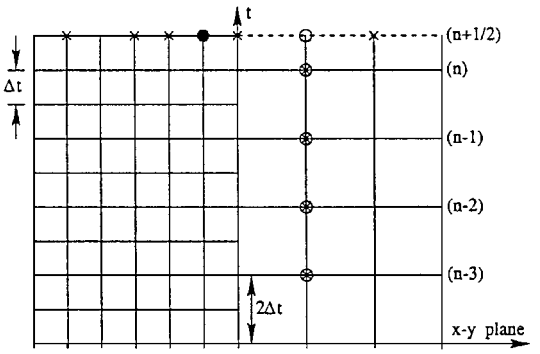

Fig. A2 Stencil to advance by a half time step: ⊘, point at which unknowns are to be found and ⊗, points of time-marching stencil.

Spatial Stencils

At the mesh size change line (Figs. A1a and A1b) every other line continues into the coarse mesh region. The other lines terminate at the mesh size change line. For points A and A', the standard seven-point symmetric DRP stencil can be used. For points B and B', C and C' symmetric stencils as shown in Fig. A1 are to be used. These stencils may be written in the form

$$\left(\frac{\partial f}{\partial x}\right)_B = \frac{1}{\Delta x}\sum_{j=-3}^{3} a_j^B f_j^B \tag{A1}$$

$$\left(\frac{\partial f}{\partial x}\right)_C = \frac{1}{\Delta x}\sum_{j=-3}^{3} a_j^C f_j^C \tag{A2}$$

The optimized stencil coefficients are

$$a_0^B = 0.0$$

$$a_1^B = -a_{-1}^B = 0.595328177715$$

$$a_2^B = -a_{-2}^B = -0.037247422191$$

$$a_3^B = -a_{-3}^B = 0.003282817772$$

$$a_0^C = 0.0, \qquad a_1^C = -a_{-1}^C = 0.726325187522$$

$$a_2^C = -a_{-2}^C = -0.120619908868$$

$$a_3^C = -a_{-3}^C = 0.003728657553$$

For points on the terminating lines, for example, A', B', and C', the stencils extend to the coarse mesh side where the values of the solution are not computed directly. They are to be found by using a six-point interpolation. For example, in Fig. A1b, the six interpolation points for the point D are D_1–D_6 as indicated by an open circle. In a recent paper, Tam and Kurbatskii[19] proposed an optimized interpolation method. This method is employed in the present investigation.

Time-Marching Stencil

To advance the solution by a half time step (as shown in Fig. A2) on the coarse mesh side, the following four levels scheme is used:

$$\boldsymbol{u}^{(n+\frac{1}{2})} = \boldsymbol{u}^{(n)} + (2\Delta t)\sum_{j=0}^{3} b_j^* \boldsymbol{K}^{(n-j)} \tag{A3}$$

where $\boldsymbol{K} = \mathrm{d}\boldsymbol{u}/\mathrm{d}t$.

A set of optimized stencil coefficients b_j^* is

$$b_0^* = 0.773100253426, \qquad b_1^* = -0.485967426944$$

$$b_2^* = 0.277634093611, \qquad b_3^* = -0.064766920092$$

Damping Stencils

The damping stencils have the same configurations as the spatial stencils. The optimized stencil coefficients used are

$$d_0^B = 0.5, \qquad d_1^B = d_{-1}^B = -0.294977493296$$

$$d_2^B = d_{-2}^B = 0.052389707989$$

$$d_3^B = d_{-3}^B = -0.007412214693$$

$$d_0^C = 0.350576727483, \qquad d_1^C = d_{-1}^C = -0.25$$

$$d_2^C = d_{-2}^C = 0.0788677598279$$

$$d_3^C = d_{-3}^C = -0.004156123569$$

Acknowledgments

This work was supported by NASA Langley Research Center Grant NAG 1-1986. Supercomputing time was provided by the SP2 Computer of the Supercomputations Research Institute and the ACNS Origin 2000 Computer of Florida State University. T. Z. Dong is acknowledged as a coauthor of the Appendix of this paper.

References

[1]Kraft, R. E., Yu, J., and Kwan, H. W., "Acoustic Treatment Impedance Models for High Frequencies," AIAA Paper 97-1653, May 1997.

[2]Hersh, A. S., and Walker, B. E., "Acoustic Behavior of Helmholtz Resonators: Part 1, Nonlinear Model," AIAA Paper 95-0078, Jan. 1995.

[3]Jones, M., "An Improved Model for Parallel-Element Liner Impedance Prediction," AIAA Paper 97-1649, May 1997.

[4]Melling, T. H., "The Acoustic Impedance of Perforates at Medium and High Sound Pressure Levels," *Journal of Sound and Vibration*, Vol. 29, No. 1, 1973, pp. 1–65.

[5]Sivian, L. J., "Acoustic Impedance of Small Orifices," *Journal of the Acoustical Society of America*, Vol. 7, 1935, pp. 94–101.

[6]Ingard, U., "On the Theory and Design of Acoustic Resonators," *Journal of the Acoustical Society of America*, Vol. 25, 1953, pp. 1037–1062.

[7]Ingard, U., and Labate, S, "Acoustic Circulation Effects and the Nonlinear Impedance of Orifices," *Journal of the Acoustical Society of America*, Vol. 22, 1950, pp. 211–219.

[8]Ingard, U., and Ising, H., "Acoustic Nonlinearity of an Orifice," *Journal of the Acoustical Society of America*, Vol. 42, 1967, pp. 6–17.

[9]Sirignano, W. A., "Nonlinear Dissipation in Acoustic Liners," AMS Rept. 553-F31-40, Princeton Univ., Princeton, NJ, 1966.

[10]Zinn, B. T., "A Theoretical Study of Non-Linear Damping by Helmholtz Resonators," *Journal of Sound and Vibration*, Vol. 13, 1970, pp. 347–356.

[11]Tam, C. K. W., and Webb, J. C., "Dispersion-Relation-Preserving Finite Difference Schemes for Computational Acoustics," *Journal of Computational Physics*, Vol. 107, Aug. 1993, pp. 262–281.

[12]Tam, C. K. W., "Computational Aeroacoustics: Issues and Methods," *AIAA Journal*, Vol. 33, No. 10, 1995, pp. 1788–1796.

[13]Shen, H., and Tam, C. K. W., "Numerical Simulation of the Generation of Axisymmetric Mode Jet Screech Tones," *AIAA Journal*, Vol. 36, No. 10, 1998, pp. 1801–1807.

[14]Tam, C. K. W., Webb, J. C., and Dong, Z., "A Study of the Short Wave Components in Computational Acoustics," *Journal of Computational Acoustics*, Vol. 1, March 1993, pp. 1–30.

[15]Tam, C. K. W., and Dong, Z., "Wall Boundary Conditions for High-Order Finite Difference Schemes in Computational Aeroacoustics," *Theoretical and Computational Fluid Dynamics*, Vol. 8, Oct. 1994, pp. 303–322.

[16]Tam, C. K. W., "Advances in Numerical Boundary Conditions for Computational Aeroacoustics," *Journal of Computational Acoustics*, Vol. 6, Dec. 1998, pp. 377–402.

[17]Tam, C. K. W., Auriault, L., and Cambuli, F., "Perfectly Matched Layer as an Absorbing Boundary Condition for the Linearized Euler Equations in Open and Ducted Domains," *Journal of Computational Physics*, Vol. 144, July 1998, pp. 213–234.

[18]Dong, Z., "Fundamental Problems in Computational Acoustics," Ph.D. Dissertation, Dept. of Mathematics, Florida State Univ., Tallahassee, FL, Spring 1994.

[19]Tam, C. K. W., and Kurbatskii, K. A., "A Wavenumber Based Extrapolation and Interpolation Method for Use in Conjunction with High-Order Finite Difference Schemes," *Journal of Computational Physics* (submitted for publication).

P. J. Morris
Associate Editor